land

MDPI

Article

Characteristics of an Inorganic Carbon Sink Influenced by Agricultural Activities in the Karst Peak Cluster Depression of Southern China (Guancun)

Ning Zhang [1], Qiong Xiao [1,2,*], Yongli Guo [1,2], Pingan Sun [1,2], Ying Miao [1,2], Fajia Chen [1,2] and Cheng Zhang [1,2,*]

[1] Key Laboratory of Karst Dynamics, Ministry of Natural Resources & Guangxi, International Research Center on Karst under the Auspices of UNESCO, National Center for International Research on Karst Dynamic System and Global Change, Institute of Karst Geology, Chinese Academy of Geological Sciences, Guilin 541004, China; angning018@gmail.com (N.Z.); gyongli@mail.cgs.gov.cn (Y.G.); sunpingan@mail.cgs.gov.cn (P.S.); miaoying@mail.cgs.gov.cn (Y.M.); fajiachen@cug.edu.cn (F.C.)

[2] Karst Ecosystem, National Observation and Research Station, Pingguo 531406, China

* Correspondence: xiaoqiong@mail.cgs.gov.cn (Q.X.); zhangcheng@mail.cgs.gov.cn (C.Z.)

Abstract: Land use in karst areas affects soil properties, impacting carbon sinks. Accurate estimation of carbon sink flux in karst areas through zoning and classification is crucial for understanding global carbon cycling and climate change. The peak cluster depression is the largest continuous karst landform region in southern China, with the depressions primarily covered by farmland and influenced by agricultural activities. This study focused on the Guancun Underground River Basin, a typical peak cluster depression basin, where sampling and analysis were conducted during the agricultural period of 2021–2022. Using hydrochemical analysis and isotopic methods, the results indicated that: (1) The primary hydrochemical type in the Guancun Underground River Basin is HCO_3-Ca, with hydrochemical composition mainly controlled by carbonate rock weathering. (2) The primary sources of Cl^-, SO_4^{2-}, and NO_3^- are agricultural activities, with agriculture contributing 0.68 mmol/L to dissolved inorganic carbon (DIC), accounting for about 13.86%, as confirmed by ion concentration analysis and isotope verification. (3) The size of the depression area is proportional to the contribution of agricultural activities to DIC, while also being influenced by dilution effects. A comparison was made regarding the contribution of other land use types to DIC. The impact of land use on DIC in karst processes should not be overlooked, and zoning and classification assessments of carbon sink flux under different influencing factors contribute to carbon peaking and carbon neutrality goals.

Keywords: peak cluster depression; agricultural activities; karst basin; land use; dissolved inorganic carbon

Citation: Zhang, N.; Xiao, Q.; Guo, Y.; Sun, P.; Miao, Y.; Chen, F.; Zhang, C. Characteristics of an Inorganic Carbon Sink Influenced by Agricultural Activities in the Karst Peak Cluster Depression of Southern China (Guancun). *Land* **2024**, *13*, 952. https://doi.org/10.3390/land13070952

Academic Editor: Nir Krakauer

Received: 10 May 2024
Revised: 18 June 2024
Accepted: 27 June 2024
Published: 28 June 2024

1. Introduction

Recently, the assessment report by the Intergovernmental Panel on Climate Change (IPCC) emphasized the gradual increase in global CO_2 gas emissions and the escalating global warming. Based on the nationally determined contributions, the projected global CO_2 emissions by 2030 could lead to a temperature increase of over 1.5 °C in the 21st century, posing a challenge to achieving the target of limiting the rise to within 2 °C [1]. In response to climate change, China has established carbon peaking and carbon neutrality goals, aiming to peak carbon emissions by 2030 and achieve carbon neutrality by 2060 [2,3]. Geological carbon sinks play a crucial role in attaining national dual carbon objectives, and karst carbon sinks are a substantial constituent of these geological carbon sinks [4–6]. As a large karst country, China boasts a wide variety of karst types and intricate structures [7,8]. It ranks first in terms of the distribution area of carbonate rocks worldwide [9]. Karst processes possess significant carbon sink capacity and potential. However, there are numerous factors influencing karst carbon sink, and accurate measurement requires the

consideration of different influencing factors through zoning and classification [10–15]. Peak cluster depression (PCD) is the most typical karst landform type in China and it is the largest continuous area of karst landforms in southern China [16,17]. Agricultural activities are the most important influencing factor in this region. Considering the impact of agricultural activities on karst processes will help measure the carbon sink more accurately [18–21].

Rivers play a vital role in carbon transport, serving as essential pathways for material cycling and energy flow. They act as connecting hubs between terrestrial and oceanic carbon reservoirs. The transfer of carbon from land to the oceans via rivers is a critical component of the global carbon cycle. Research suggests that approximately 1.0 Gt C a^{-1} carbon enters the oceans through rivers each year [22]. Various human activities, such as industrial and agricultural production, generate a large amount of nitrogen (N) and sulfur (S) compounds, which undergo a series of reactions to transform into sulfuric and nitric acid etc. in the natural environment [20,23–25]. These acids in rivers participate in the weathering of carbonate rocks, leading to a significant increase in HCO_3^- in the groundwater [26–28]. However, this increase does not consume CO_2 from the atmosphere or soil. Instead, it lowers the pH of the river, resulting in a deviation in carbon sink measurement [12,29]. Anderson indicates that sulfuric acid, resulting from the oxidation of pyrite (FeS_2) accounts for about 20% of the total dissolution of carbonate rocks in glacial environments [30]. Perrin found that the application of nitrogen fertilizers reduced the dissolution of carbonates in carbonate rocks by approximately 10% through comparative studies in agricultural regions [18]. Jiang found that exogenous acid dissolution of carbonate rocks leads to an increase in the concentrations of ions such as Ca^{2+}, Mg^{2+}, and HCO_3^- in the river water through their research on the underground river in Laolongdong, Nanshan, Chongqing [31]. Sun estimated that the contribution range of exogenous acid dissolution of carbonate rocks to inorganic carbon is approximately 10% to 30% in the Lijiang Basin [32]. Therefore, considering the interference of natural conditions and human activities, the contribution of sulfuric and nitric acid weathering dissolution to inorganic carbon in carbonate rocks cannot be overlooked. Specifically, exogenous acids have an impact on reducing carbon sinks and must be subtracted from the calculation of the karst carbon sink [33]. Scientific research assesses the impacts of sulfuric and nitric acid on the weathering of carbonate rocks and carbon cycling. This analysis is vital for accurately estimating carbon sinks and improving our understanding of global carbon cycling mechanisms across different geographic areas and conditions [34,35].

Karst landforms are widely distributed and more abundant in the typical karst region of southwest China [15,36]. The unique dual structure of surface and subterranean features facilitates the influx of external substances, thereby accelerating the weathering of carbonate rocks in karst regions. The inflow of sulfuric and nitric acid accelerates the weathering rate of carbonate rocks, resulting in an increase in dissolved inorganic carbon (DIC) concentration in rivers. However, there is no consumption of CO_2 in this process and no carbon sink process occurs [20]. The Guancun Underground River Basin is a typical karst PCD landform in southwest China. In geology, the stratigraphic sequence consists of Upper Devonian Rong'an Formation limestone and dolomitic limestone [37]. Previous research has extensively studied the use of Na^+, K^+, Mg^{2+}, Ca^{2+}, HCO_3^-, Cl^-, SO_4^{2-}, and NO_3^- to indicate the sources and composition of ions, analyze the weathering process of carbonate rocks, and calculate carbon sink intensity [18–20]. Guo analyzed the concentration trends and sources of major ions in the basin and estimated the carbon sink intensity of the Guancun Underground River Basin as 12.34 tC·km^{-2}·a^{-1} using the hydrochemical runoff method [38]. However, these studies did not consider the land use patterns in depressions, nor the impact of exogenous acids from agricultural activities on the weathering of carbonate rocks [20,39]. Therefore, this paper uses the Guancun Underground River Basin as a research object. The objectives of the research are to: (1) analyze the hydrochemical characteristics of the basin and the major ion sources; (2) determine agricultural activities as the primary sources of Cl^-, SO_4^{2-}, and NO_3^- through ion correlations and isotopic ver-

ification; (3) calculate the proportion of sulfuric and nitric acid generated from agricultural activities that contribute to carbonate rock weathering; (4) Compare the influence of various land use types on karst carbon sinks in different karst landforms. The goal of this study is to improve the precision of inorganic carbon flux assessment in the PCD landform basin's water system, providing a theoretical basis for estimating carbon sink capacities in karst critical zones in Southwest China. Furthermore, it offers insights into the measurement of karst carbon sinks through zoning and classification.

2. Materials and Methods

2.1. Study Area

The Guancun Underground River Basin is located north of Daliang Town, Rong'an County, Liuzhou City, Guangxi (coordinates: 109°19′ E~109°23′ E, 24°84′ N~24°87′ N). The basin has an area of 30.5 km^2 [40] and is a typical karst PCD landform. The terrain is higher in the northeast, with an average elevation of about 420 m. The geological formation of the area consists of the Upper Devonian Rong'an Formation (D_3r), which comprises medium-thickness layers of limestone with interbedded dolomite. The thickness of the formation ranges from 606 to 1202 m [41]. The depression is elongated in shape and developed along the axis of the anticline fold. The underground river channel is controlled by secondary vertical extension fractures along the axis of an anticline fold. Surface landforms such as funnels, uvala, poljes, and underground river skylights are extensively developed in the area, along with underground features such as conduits, karst caves, and underground rivers. The Guancun underground river originates in the northeastern, in a sinkhole on the edge of a depression of siliceous rock. It flows underground for about one kilometer between the mountains and then resurfaces as a surface river at Shanghudong (SHD). At surface, the northern branch of the river flows northwest and leaves the basin, while the southern branch continues along the main stream, passing through Xiahudong (XHD) and Macao (MC), and resurfaces again at Macao. After one kilometer of open flow, it rejoins the southernmost sinkhole and goes underground again. It then joins the eastern conduit and eventually discharges at the outlet of the underground river in eastern Shankou (SK) Village (Figure 1a). The profile diagram (Figure 1b) is drawn along the A-B profile. In the basin, agriculture is predominantly characterized by paddy fields, with major crops including grass seedlings, rice, corn, and sugarcane. Fertilization occurs three times during the farming season, which spans from April to September. Fertilizers, including compound fertilizer with an average application rate of around 1000 $kg{\cdot}hm^{-2}$ and urea with an average application rate of approximately 375 $kg{\cdot}hm^{-2}$ are applied in April, May, and September [42].

2.2. Sampling and Analytical Methods

The water samples from the Guancun Underground River Basin collected by the project team during the agricultural period of 2021–2022. A total of 8 sampling points was selected, comprising 5 karst windows: Shanghudong (SHD) Karst Window (GC1), Xiahudong (XHD) Window (GC3), Macao (MC) Karst Window (GC4), Mengdong (MD) Overflow Window (GC5), and Dayantan (DYT) Karst Window (GC7); 2 karst springs: Legang (LG) Surface Karst Spring (GC2) and Xizhailiao (XZL) Surface Karst Spring (GC6); and 1 underground river outlet: Shankou (SK) Village Underground River Outlet (GC8). The distribution of the sampling points is illustrated in Figure 1. On-site measurements of pH, Total Dissolved Solids (TDS), and other river water parameters at the sampling points were conducted using a portable water quality multi-parameter analyzer (YSI692). The accuracy of the measurements was 0.01 pH units and 0.1 mg/L, respectively. For laboratory testing of cations, anions, and isotopes ($\delta^{15}N\text{-}NO_3^-$, $\delta^{18}O\text{-}NO_3^-$, and $\delta^{13}C_{DIC}$), water samples were collected in polyethylene bottles that had been pre-cleaned with deionized water. During cation sampling, three drops of 1:1 nitric acid solution were added to acidify the samples to pH < 2. Following carbon isotope sampling, saturated $HgCl_2$ solution was promptly added to inhibit microbial activity, and the bottle caps were sealed with sealing film. All samples

were stored in a refrigerated environment at 4 °C after collection and analyzed within 7 days.

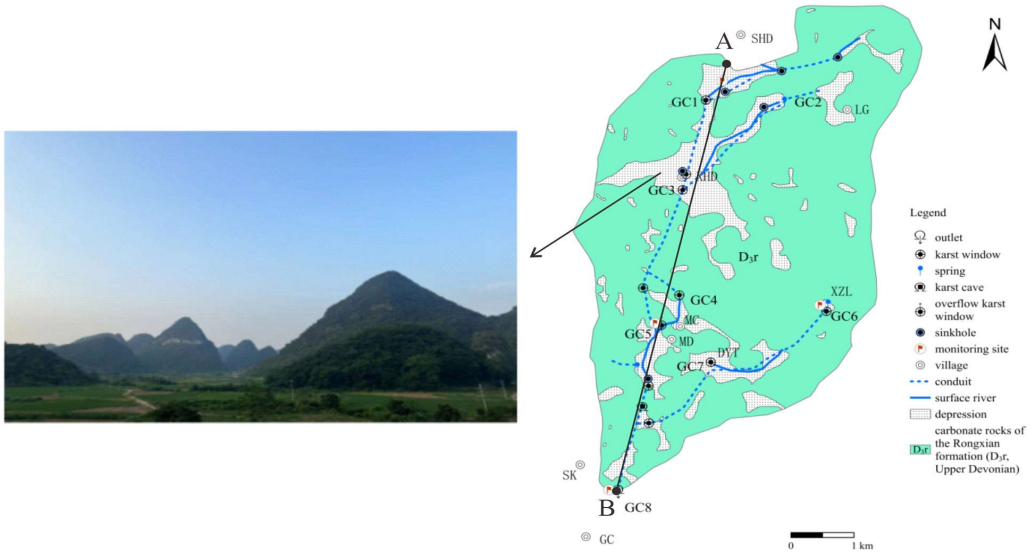

(**a**)

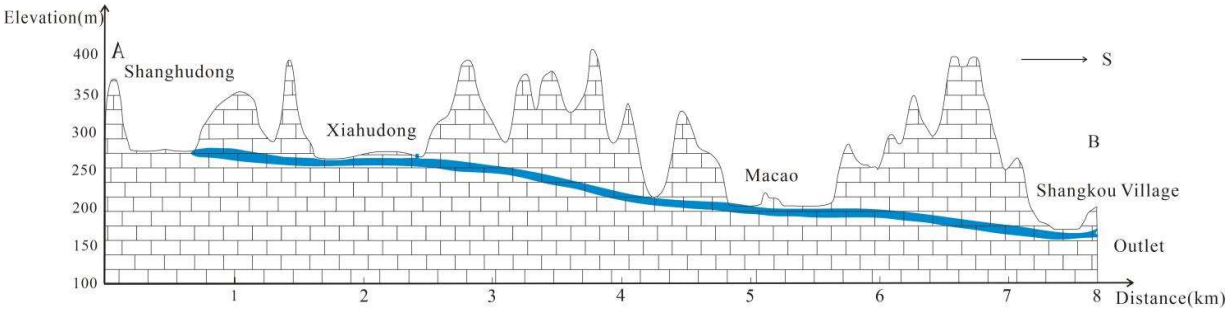

(**b**)

Figure 1. Study area (**a**) sampling points; (**b**) hydrogeological profile map from A to B.

The cations (K^+, Na^+, Ca^{2+}, Mg^{2+}) in the collected water samples were analyzed in the laboratory using an Optima 2100DV ICP-OES spectrometer (PerkinElmer, Waltham, MA, USA), with a measurement accuracy of 0.01 mg/L. The anions (Cl^-, $NO_3{}^-$, $SO_4{}^{2-}$) in the water samples were analyzed using a Dionex ICS-900 ion chromatograph (Thermo Fisher Scientific, Waltham, MA, USA) with a measurement accuracy of 0.01 mg/L. The measurement error was within ±5%. The total equivalent concentration of cations is represented as TZ^+ ($TZ^+ = Na^+ + K^+ + 2Mg^{2+} + 2Ca^{2+}$), and the total equivalent concentration of anions is represented as TZ^- ($TZ^- = Cl^- + 2SO_4{}^{2-} + NO_3{}^- + HCO_3{}^-$). The inorganic cation-anion charge balance is represented as NICB ($[NICB = (TZ^+ - TZ^-) \times 100/TZ^-]$). Carbon isotopes were analyzed using a MAT253 stable isotope mass spectrometer (Thermo Fisher Scientific, Bremen, Germany) with a measurement accuracy of ±0.01‰. The results were reported based on the V-PDB standard. The laboratory testing mentioned above was performed by the Geological and Environmental Testing Center, Institute of Karst Geology, Ministry of Natural Resources, in Guilin, Guangxi, China. The hydrochemical data underwent cluster analysis using IBM SPSS Statistics 26.0 software. The analysis of nitrogen and oxygen isotopes was conducted using the denitrification bacteria method. Denitrifying bacteria converted $NO_3{}^-$ to N_2O gas, which was subsequently separated, purified, and captured using a Trace Gas analyzer equipped with a Gilson autosampler. The isotopic values of N and O in N_2O were determined using an isotope ratio mass

spectrometer. The isotopic values of N and O were referenced to atmospheric N_2 and Vienna Standard Mean Ocean Water (V-SMOW), respectively. The measured gases were calibrated using a two-point calibration method, resulting in a measurement accuracy of 0.01‰. The analysis was carried out by the Third Institute of Oceanography, Ministry of Natural Resources, in Xiamen, Fujian Province, China. To accurately determine the river flow rates, a flow meter and a water level gauge were deployed at the river outlet. The flow meter was utilized to measure the velocity of the water flow, while the water level gauge monitored the height of the water level. Together with the geometric characteristics of the river cross-section, these measurements allowed for the effective calculation of the river's instantaneous flow rate, which was then averaged to obtain daily flow values. The placement and setup of these measuring devices were strategically chosen to ensure the accuracy and representativeness of the data, thereby supporting the reliability of the study results.

3. Results

3.1. Analysis of Hydrochemical Characteristics

TZ^+ in the water samples obtained from the Guancun Underground River varied between 4.50 and 6.87 meq/L, with an average value of 5.32 meq/L. Similarly, TZ^- ranged from 4.50 to 6.97 meq/L, with an average value of 5.30 meq/L. The difference between cations and anions in terms of charge balance was less than 5%, indicating a relatively balanced composition of ions. NICB can serve as an assessment of the reliability of the hydrochemical analysis results or the level of water contamination. Based on the hydrochemical data parameters of the Guancun groundwater samples, the NICB values varied from −3.99% to 4.62%. Figure 2 illustrates the relationship between TZ^+ and TZ^-, showing a linear fit with a correlation coefficient of $R^2 = 0.981$, indicating a nearly balanced total charges of cations and anions. The analysis results for various ions demonstrate a relatively high level of reliability.

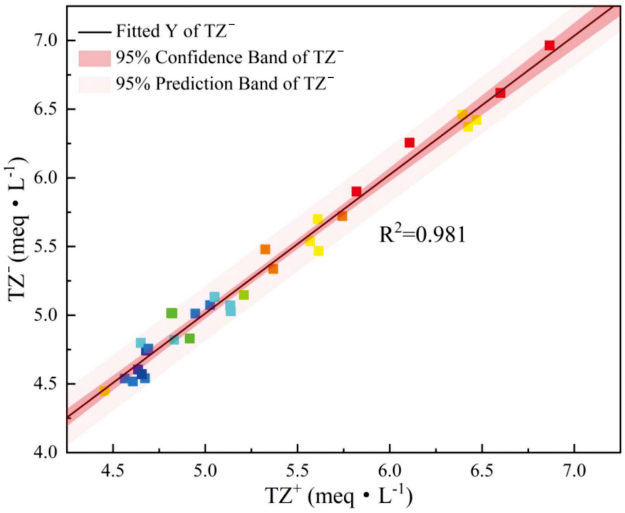

Figure 2. Anion and cation balance of the Guancun Underground River.

The ion concentrations detected in the Guancun Underground River are presented in Table 1. Among the cations, Ca^{2+} exhibits the highest concentration, followed by Mg^{2+}, Na^+, and K^+. Ca^{2+} and Mg^{2+} are the dominant cations, with concentration ranges of 69.32 to 98.90 mg/L and 6.75 to 27.90 mg/L, respectively. Together, they account for 98.45% of the total cation content. Regarding the anions, HCO_3^- is the primary species, with a concentration range of 248.6 mg/L to 400.1 mg/L, representing 92.46% of the total anion concentration. The subsequent anions are SO_4^{2-} and NO_3^-, with concentration ranges of 7.17 to 18.35 mg/L and 0.05 to 21.91 mg/L, respectively.

Table 1. Chemical composition of Guancun Underground River.

Date	Site	pH	K^+ mg/L	Na^+ mg/L	Ca^{2+} mg/L	Mg^{2+} mg/L	Cl^- mg/L	SO_4^{2-} mg/L	NO_3^- mg/L	HCO_3^- mg/L	TDS mg/L	$\delta^{15}N\text{-}NO_3^-$ ‰	$\delta^{18}O\text{-}NO_3^-$ ‰	$\delta^{13}C_{DIC}$ ‰
April 2021	GC1	7.36	0.17	0.59	88.53	14.17	0.83	8.26	2.23	319.50	232.6	2.84	−2.54	−15.42
	GC2	7.26	0.05	0.57	89.13	23.70	0.96	10.70	0.12	373.50	269.7	7.20	8.33	−16.87
	GC3	7.31	0.88	2.09	98.06	8.95	3.96	13.59	19.32	306.00	212.3	2.16	−4.94	−13.76
	GC4	7.58	0.88	1.53	83.06	10.95	2.06	9.90	9.96	283.50	245.6	2.31	−3.73	−13.19
	GC5	7.59	0.86	1.44	83.20	10.96	2.04	9.78	9.88	281.25	217.8	2.31	−3.42	−14.06
	GC6	7.46	0.08	0.77	84.19	27.14	1.86	10.52	12.01	363.38	270.5	2.31	−3.74	−15.95
	GC7	–	–	–	–	–	–	–	–	–	–	–	–	–
	GC8	7.68	0.83	1.26	83.24	11.90	2.29	10.00	9.61	288.00	230.1	3.09	−6.25	−13.21
June 2021	GC1	7.18	0.48	0.51	74.82	11.07	1.01	13.43	<0.05	270.58	209.8	17.93	25.40	−15.90
	GC2	7.16	0.21	0.70	86.05	21.60	1.58	13.86	7.66	353.84	275.9	1.79	20.83	−16.67
	GC3	7.08	0.55	1.71	92.48	11.01	6.34	15.60	21.91	295.56	262.2	6.02	3.94	−13.28
	GC4	7.27	0.56	1.09	78.36	10.32	5.04	14.68	12.40	266.42	221.9	20.94	−7.79	−14.15
	GC5	7.04	0.52	1.05	78.68	10.10	5.00	14.57	<0.05	278.91	221.3	31.40	−2.89	−14.27
	GC6	7.48	0.07	0.82	82.29	27.33	1.60	13.63	12.13	362.16	290.8	5.38	−0.04	−16.57
	GC7	7.20	0.27	0.85	85.26	12.48	5.63	14.08	17.77	289.32	246.7	4.14	−0.55	−14.90
	GC8	7.75	0.44	0.94	76.62	9.42	5.20	14.53	11.67	253.93	220.4	5.58	−1.72	−13.75
September 2021	GC1	7.42	1.10	1.13	69.32	13.02	1.21	14.32	<0.05	255.38	206.0	9.93	2.59	−14.48
	GC2	7.30	0.04	0.82	98.09	23.51	0.99	13.41	6.30	400.02	305.4	5.21	7.13	−17.05
	GC3	7.50	0.68	2.20	95.85	11.22	6.43	17.44	20.97	306.23	268.1	5.32	1.27	−13.01
	GC4	7.37	0.67	1.48	82.13	10.28	5.08	16.16	9.28	271.20	230.6	5.55	−0.61	−14.01
	GC5	7.39	0.93	1.24	77.90	8.82	5.16	16.38	12.22	248.60	230.2	5.98	2.60	−14.20
	GC6	7.28	0.16	0.83	89.64	17.86	5.72	15.85	7.87	299.36	2454	5.46	−3.65	−14.23
	GC7	–	–	–	–	–	–	–	–	–	–	–	–	–
	GC8	7.54	0.55	1.07	83.42	10.05	5.36	15.14	13.82	271.20	233.7	4.62	−0.55	−13.50
April 2022	GC1	7.35	0.12	0.49	74.93	9.72	1.72	11.66	1.84	257.42	199.2	2.37	0.96	−15.22
	GC2	–	–	–	–	–	–	–	–	–	–	–	–	–
	GC3	7.36	0.72	2.04	94.14	9.27	5.38	18.35	17.59	288.06	115.9	4.78	3.96	−13.14
	GC4	7.29	0.51	0.96	78.33	8.62	2.48	13.96	2.85	252.31	209.6	−0.42	−12.99	−13.49
	GC5	7.21	0.46	0.93	77.86	8.48	2.46	13.80	10.12	249.25	210.2	3.71	0.12	−13.66
	GC6	7.08	0.10	0.82	86.82	27.08	2.20	12.28	12.83	371.83	289.3	3.47	1.88	−16.03
	GC7	7.16	0.21	0.83	88.46	11.09	5.34	11.86	18.74	282.96	241.3	3.10	1.44	−14.25
	GC8	7.70	0.56	0.93	78.39	8.38	2.66	13.76	5.72	251.29	210.2	4.61	2.51	−13.36
June 2022	GC1	7.29	1.40	0.73	73.63	8.66	0.88	11.66	<0.05	255.14	199.0	6.94	5.97	−15.12
	GC2	–	–	–	–	–	–	–	–	–	–	–	–	–
	GC3	7.19	0.44	0.83	84.49	7.93	1.56	15.19	0.52	272.27	220.3	3.96	2.20	−14.36
	GC4	7.28	0.44	0.78	83.99	7.23	1.44	13.81	<0.05	274.18	213.8	4.02	−0.21	−15.10
	GC5	7.26	0.36	0.75	87.15	6.75	1.55	13.10	6.78	279.89	220.7	3.96	0.81	−15.54
	GC6	7.35	0.15	0.69	79.46	21.37	1.02	10.20	6.11	333.20	249.3	4.60	1.99	−15.90
	GC7	7.28	0.37	0.82	83.36	14.58	5.74	13.88	16.98	281.72	248.7	4.56	−0.35	−15.05
	GC8	7.69	0.47	0.83	85.21	7.40	1.76	13.01	5.68	271.32	217.8	3.65	4.76	−14.48
September 2022	GC1	7.30	0.78	0.64	76.46	13.17	0.80	7.17	0.51	277.96	219.6	4.30	−2.70	−15.32
	GC2	–	–	–	–	–	–	–	–	–	–	–	–	–
	GC3	6.92	0.41	1.26	92.37	11.90	3.68	13.47	18.23	297.00	256.7	3.81	−0.68	−12.91
	GC4	6.96	0.55	0.98	83.55	11.35	2.21	12.85	7.68	274.15	127.6	5.83	1.95	−14.09
	GC5	6.96	0.58	0.97	83.24	11.69	2.16	12.94	9.54	274.15	230.3	5.23	2.33	−14.03
	GC6	6.88	0.08	0.74	86.38	27.90	1.22	8.25	6.97	369.34	285.9	3.46	−4.25	−16.23
	GC7	6.92	0.20	0.78	88.92	13.41	3.09	8.79	15.98	293.19	248.4	2.72	−1.12	−14.70
	GC8	7.07	0.59	0.95	84.22	10.17	2.40	12.87	9.67	272.25	228.2	5.96	2.07	−13.95

Piper and Durov diagrams are commonly employed methods for evaluating hydrochemical types. The Piper diagram provides information on the relationship between water composition and rock types, while the Durov diagram elucidates how geochemical processes impact groundwater [43,44]. In Figure 3a, the Piper diagram illustrates that the total alkaline metal ions Ca^{2+} and Mg^{2+} surpass the total Na^+ and K^+, and the weak acid radicals HCO_3^- and CO_3^{2-} exceed the strong acid radicals SO_4^{2-} and Cl^-. Figure 3b, presenting the Durov diagram, demonstrates that the majority of constituents in the water are alkaline dissolved solids. Dissolution emerges as the principal process shaping the hydrochemical characteristics of the samples, signifying a noteworthy influence of alkaline rocks on water chemistry. The ion distribution and concentration in the Guancun Underground River Basin are relatively consistent, indicating a limited range of variation in ion concentrations. Among cations, Ca^{2+} holds the highest concentration, constituting an average of 85.37% of the total cations. Among anions, HCO_3^- exhibits the highest concentration, accounting for

an average of 91.56% of the total anions. To comprehensively analyze the karst groundwater sources in the study area, the water samples demonstrate a consistent hydrochemical type known as HCO_3−Ca type.

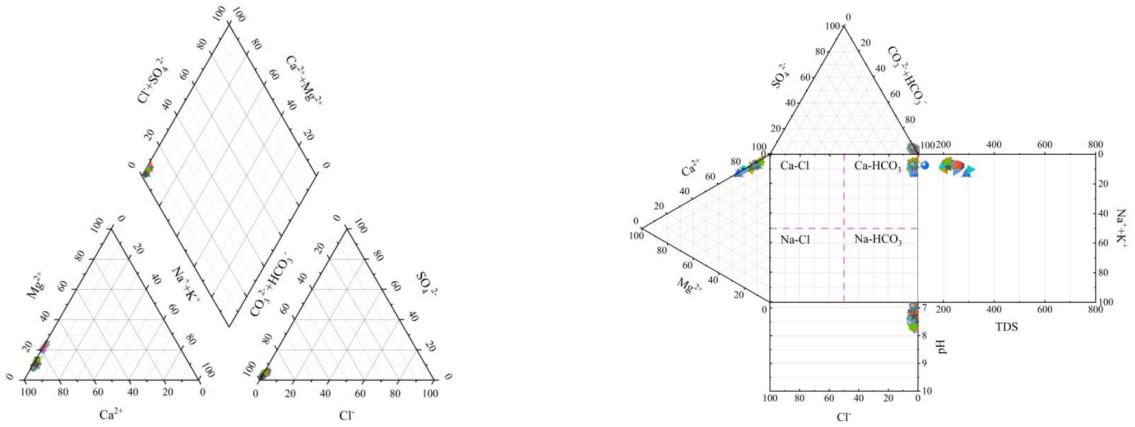

(**a**) (**b**)

Figure 3. Basin water phase characteristics Piper (**a**) and Durov (**b**) diagrams.

3.2. Analysis of Ion Sources

To comprehensively analyze the sources of karst groundwater in the study area, hydrochemical data were subjected to cluster analysis using the software IBM SPSS Statistics 26.0. The cluster analysis dendrogram (Figure 4) was generated with the average linkage method and squared Euclidean distance, following data standardization. Correlation according to ions: the ions can be categorized into two clusters, namely Type I blue and Type II red. Type I ions, including Ca^{2+}, Mg^{2+}, and HCO_3^-, dominate the ion composition. These ions likely originate from carbonate rock weathering. Type II ions consist of Na^+, K^+, Cl^-, SO_4^{2-}, and NO_3^-. The concentrations of Na^+ and K^+ remain within permissible limits, while Cl^-, SO_4^{2-}, and NO_3^- may share a common source. Given the predominance of limestone and dolomitic limestone, coupled with the presence of typical peak cluster depression landforms and minimal industrial activities, it is possible that the source of Cl^-, SO_4^{2-}, and NO_3^- ions may be due to agricultural activities and atmospheric acid deposition.

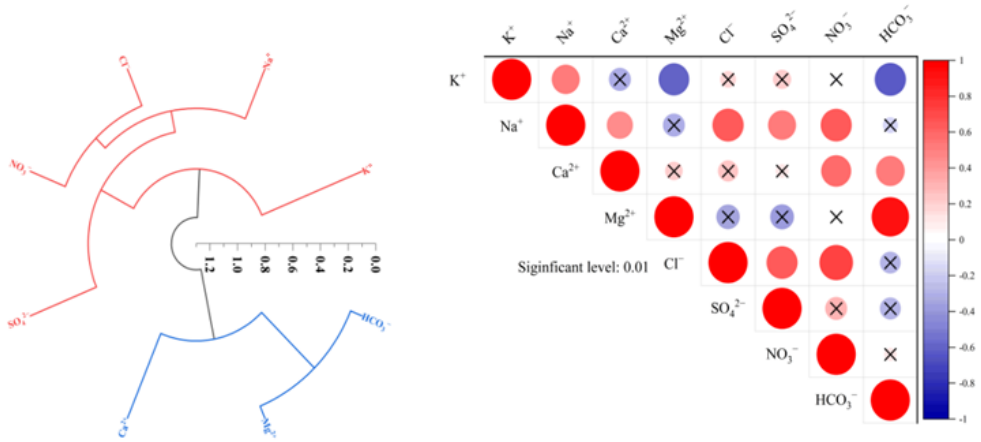

Figure 4. Cluster analysis dendrogram and correlation plot.

3.2.1. Determining the Primary Source of Ions in the Water

The Gibbs diagram is a valuable tool for studying hydrogeochemical processes, allowing the classification of controlling mechanisms of river water chemistry into three types: "evaporation concentration type" (ECT), "rock weathering type" (RWT), and "atmospheric precipitation type" (APT). Figure 5 demonstrates that TDS in the Guancun

Underground River Basin ranges from 248.6 to 400.2 mg/L, indicating relatively low content. The $Na^+/(Na^+ + Ca^{2+})$ ratio ranges from 0.001 to 0.069, and the $Cl^-/(Cl^- + HCO_3^-)$ ratio ranges from 0.002 to 0.021. Both ratios are below 0.5, with a majority of data points aligning with the RWT, emphasizing its dominance in river water composition. The hydrochemical characteristics of the Guancun Underground River Basin primarily originate from the weathering of carbonate rocks.

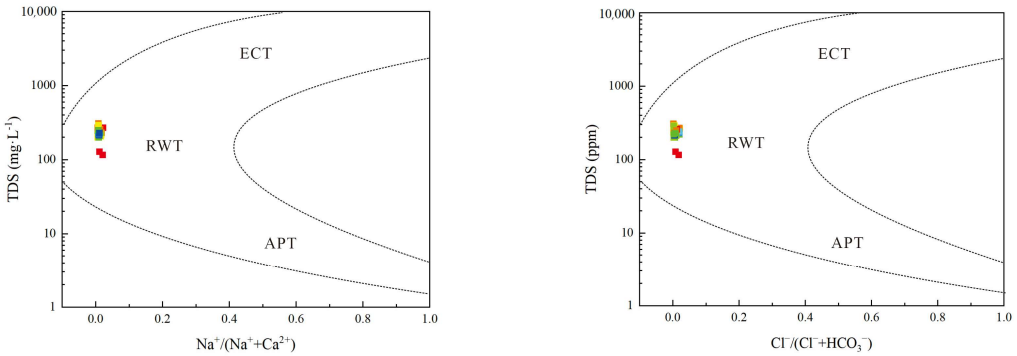

Figure 5. Map of water chemistry control mechanisms.

The relationship between Mg^{2+}/Na^+ and Ca^{2+}/Na^+, as well as HCO_3^-/Na^+ and Ca^{2+}/Na^+, further supports this point. Ca^{2+}, Mg^{2+}, Na^+, and HCO_3^- originate from distinct sources, and there are differences in their abundance. The relationship can be summarized as follows: Na^+ abundance originates primarily from evaporation-related weathering, followed by silicate weathering, and then carbonate weathering. On the other hand, Ca^{2+}, Mg^{2+}, and HCO_3^- abundance stems primarily from carbonate weathering, followed by silicate weathering, and then evaporite weathering. To determine the predominant type of rock weathering in the Guancun Underground River Basin, a qualitative analysis can be conducted by plotting the ratios of Ca^{2+}/Na^+ and Mg^{2+}/Na^+, as well as Ca^{2+}/Na^+ and HCO_3^-/Na^+, for different sampling points. Figure 6 illustrates that the sampling points are concentrated and all fall within the carbonate weathering end-member. Considering that the predominant bedrock in the study area is limestone and dolomitic limestone, it can be concluded that carbonate weathering, specifically from limestone and dolomitic limestone, is the primary source of the hydrochemical composition in the basin.

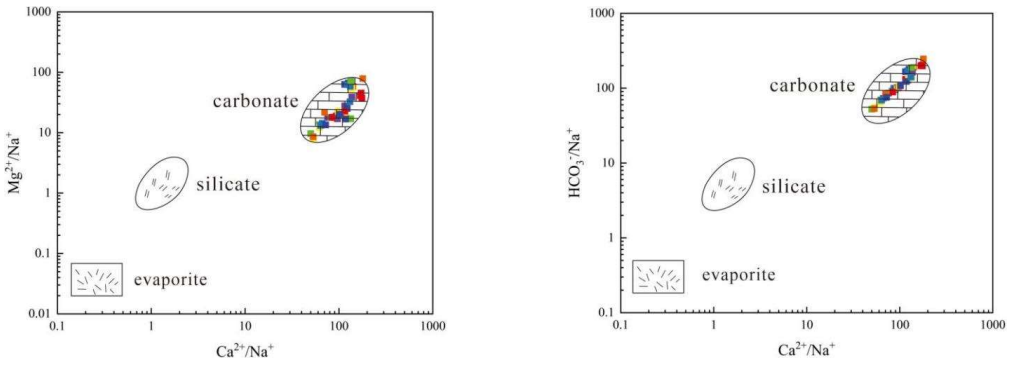

Figure 6. Rock weathering end-element diagram.

3.2.2. Investigating the Primary Sources of Cl^-, SO_4^{2-} and NO_3^- in Water

Cluster analysis indicates that the type II ion comprises Cl^-, SO_4^{2-}, and NO_3^-. Figure 7 illustrates that the variations Cl^-, SO_4^{2-}, and NO_3^- exhibit consistent trends and spatial distribution characteristics across different sampling points. Notably, sampling points GC3, GC5, and GC8 demonstrate higher concentrations of these three ions. These findings strongly suggest that Cl^-, SO_4^{2-}, and NO_3^- likely originate from common sources.

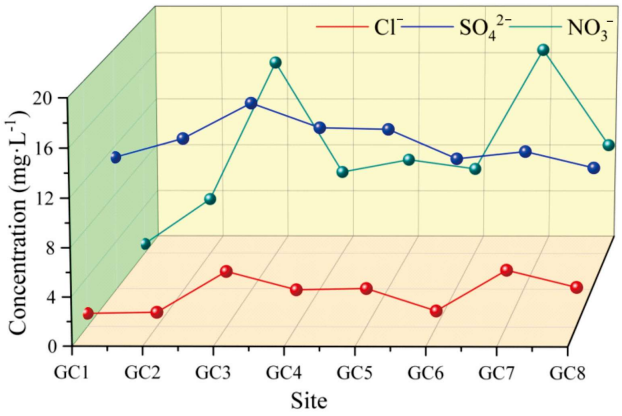

Figure 7. Trends in Cl^-, SO_4^{2-} and NO_3^-.

The correlation between NO_3^- and Cl^- derived from various sources serves as an indicator for distinguishing the origin of nitrate. The NO_3^-/Cl^- ratio is instrumental in identifying the source of NO_3^-. A high NO_3^-/Cl^- ratio coupled with low Cl^- levels suggests an agricultural origin, whereas a low NO_3^-/Cl^- ratio combined with high Cl^- levels indicates sources such as animal manure and domestic wastewater. When both the NO_3^-/Cl^- ratio and Cl^- are low, it indicates atmospheric deposition. Figure 8a shows a scatter plot of Cl^- against the NO_3^-/Cl^- ratio for the sampling points, utilizing a color density mapping distribution. The concentration of colors in the region, characterized by a high NO_3^-/Cl^- ratio and low Cl^-, signifies that the primary source of NO_3^- is agricultural activities.

Sulfate (SO_4^{2-}) in water primarily originates from gypsum dissolution, sulfide oxidation, and anthropogenic inputs. However, given the lack of sulfur in the strata, the absence of sulfate deposition, and no sulfide deposits found during the field investigation and sampling process, the contribution of carbonate rocks to the groundwater SO_4^{2-} concentration can be neglected. Therefore, the SO_4^{2-} primarily originates from anthropogenic inputs. The analysis of the SO_4^{2-} source can also utilize the ratios of SO_4^{2-}/Ca^{2+} and NO_3^-/Ca^{2+}. The relationship among SO_4^{2-}, NO_3^-, and Ca^{2+} ratios facilitates the differentiation of the impact of various human activities on surface water. A high SO_4^{2-}/Ca^{2+} ratio suggests a predominant influence of mining activities, while a high NO_3^-/Ca^{2+} ratio indicates a significant impact from agricultural activities. The underlying lithology does not contain sulphate rock. Figure 8b illustrates the ratio relationship between SO_4^{2-}/Ca^{2+} and NO_3^-/Ca^{2+}, with the sampling point data showing lower SO_4^{2-}/Ca^{2+} ratios predominantly on the side associated with agricultural activities. This observation indicates that agricultural activities primarily influence the SO_4^{2-} content in the basin, which aligns with the inferred conclusions. Previous collection and analysis of rainwater in this area have been conducted, revealing that the concentrations of SO_4^{2-} ions range from 5 to 8 mg/L and NO_3^- ions from 1 to 3 mg/L. Findings suggest the presence of soil buffering, which excludes the contribution of atmospheric acid deposition to river ion concentrations.

To further ascertain agricultural activities as the second influential factor on ion hydrochemical characteristics in the basin, the utilization of $\delta^{15}N\text{-}NO_3^-$ and $\delta^{18}O\text{-}NO_3^-$ isotopic values is necessary for source identification of NO_3^-. However, it is imperative to first identify denitrification processes, as isotopic fractionation can impact source identification of NO_3^-. Figure 8c shows the relationship between NO_3^- concentration and $\delta^{15}N\text{-}NO_3^-$ values.

The linear regression analysis showed $R^2 = 0.161$, indicating a limited influence of denitrification processes, as the $\delta^{15}N\text{-}NO_3^-$ values did not exhibit a significant increase with decreasing NO_3^- concentration, highlighting the feasibility of utilizing isotopic fingerprinting for source identification of NO_3^-. In Figure 8d, the $\delta^{15}N\text{-}NO_3^-$ and $\delta^{18}O\text{-}NO_3^-$ isotopic values of the sampling points in the basin are visualized through a color density mapping distribution projected onto the NO_3^- source interval. The scattered red points

may indicate isotopic fractionation, and their impact on result accuracy should be disregarded. The remaining points are distributed within the overlapping interval of NH_4^+ fertilizers and soil organic nitrogen. Interviews conducted with local farmers revealed that compound fertilizers commonly used during agricultural activities contain NH_4^+, including urea ($CO(NH_2)_2$), potassium sulfate (K_2SO_4), ammonium sulfate ($(NH_4)_2SO_4$), diammonium phosphate ($(NH_4)_2HPO_4$), potassium chloride (KCl), and other components. This aligns with the distribution range of experimental data, indicating that both NH_4^+ fertilizers and soil organic nitrogen, derived from agricultural activities, contribute to the main source of NO_3^- ions in the basin.

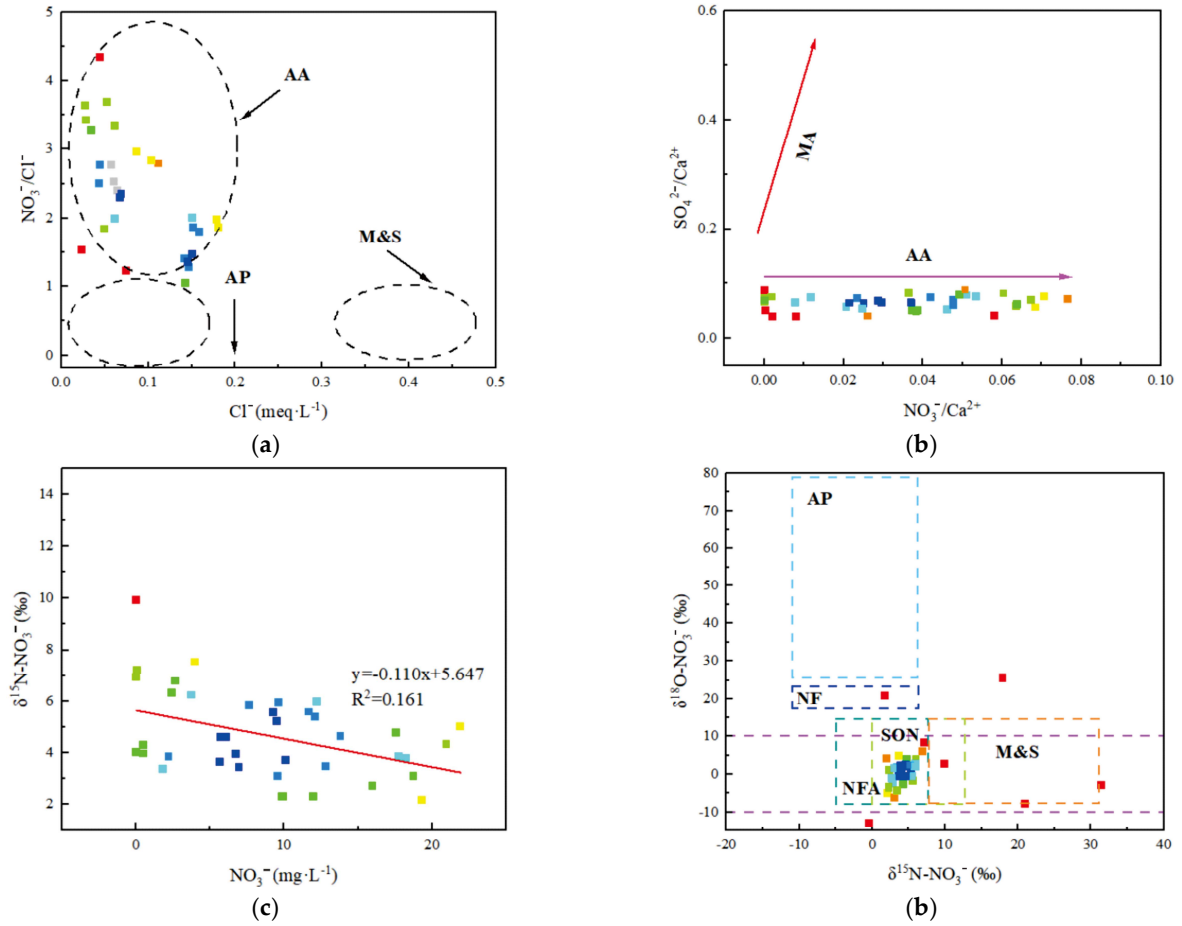

Figure 8. Subfigures (**a**,**c**,**d**) depict the sources for NO_3^-, and Subfigure (**b**) represents the source for SO_4^{2-}.

Based on the analysis conducted using ion correlation and isotopic methods to identify the sources of Cl^-, SO_4^{2-}, and NO_3^- ions, along with a comprehensive geological assessment of the Guancun Underground River Basin, the results indicate a possible linkage between the identified ions and their geological sources. The sources of these three ions show consistency in terms of variation trends and spatial distribution, all of which are attributed to agricultural activities. Atmospheric sulfur emissions have significantly decreased due to regulatory measures, yet there is a substantial addition of reactive sulfur to agricultural lands in the form of fertilizers, pesticides, and soil conditioners [45]. The input of nitrogen and sulfur from agricultural activities cannot be ignored. The compound fertilizer used in farming in this area contains sulfur fertilizer and nitrogen fertilizer, and the specific reaction process is as follows:

$$\begin{aligned} NH_4^+ + 1.5O_2 &\rightarrow NO_2^- + 2H^+ + H_2O \\ NO_2^- + 0.5O_2 &\rightarrow NO_3^- \end{aligned} \quad (1)$$

$$\begin{aligned} &S + 1.5O_2 + H_2O \rightarrow H_2SO_4 \\ &H_2S + 2O_2 \rightarrow H_2SO_4 \\ &H_2SO_4 \rightarrow 2H^+ + SO_4^{2-} \end{aligned} \quad (2)$$

4. Discussion

4.1. Contribution of Agricultural Activities to Carbonate Rock Weathering

The hydrochemical characteristics of the Guancun Underground River Basin are primarily influenced by the weathering process of carbonate rocks. The weathering of carbonate rocks involves the dissolution of carbonates through the action of carbonic, sulfuric and nitric acid, as expressed by the following equations:

$$Ca_xMg_{1-x}CO_3 + H_2CO_3 \rightarrow xCa^{2+} + (1-x)Mg^{2+} + 2HCO_3^- \quad (3)$$

$$2Ca_xMg_{(1-x)}CO_3 + H_2SO_4 \rightarrow 2xCa^{2+} + 2(1-x)Mg^{2+} + 2HCO_3^- + SO_4^{2-} \quad (4)$$

$$Ca_xMg_{(1-x)}CO_3 + H_2NO_3 \rightarrow xCa^{2+} + (1-x)Mg^{2+} + HCO_3^- + NO_3^- \quad (5)$$

Equation (1) depicts the carbonate weathering process through carbonic acid. Equations (2) and (3) involve the participation of sulfuric and nitric acid in the chemical weathering of rocks without any CO_2 consumption, thus lacking a carbon sink process. Despite not consuming CO_2, the weathering process of carbonate rocks through sulfuric and nitric acid generates $HCO_3{}^-$. This distinction is crucial as it impacts the overall carbon balance in weathering reactions. When quantifying the carbon sink, this contribution should be subtracted. Agricultural activities constitute the primary influencing factor in the Guancun Underground River Basin. The presence of $SO_4{}^{2-}$ and $NO_3{}^-$ in the basin primarily stems from agricultural activities. Hence, during the calculation of carbon sequestration in this basin, the quantity of sulfuric and nitric acid generated by agricultural activities involved in the chemical weathering of carbonate rocks should be subtracted.

Based on Table 1, the pH values across different sampling points within the Guancun Underground River Basin range from 6.88 to 7.75, with an average of 7.30. DIC in the river water mainly comprises $CO_3{}^{2-}$, $HCO_3{}^-$, and dissolved CO_2. Within the pH range of 6.4 to 10.3, $HCO_3{}^-$ predominantly constitute DIC. As the pH in the basin hovers around 7.30, DIC serves as a representative of $HCO_3{}^-$. Hydrochemical equilibrium methods are frequently employed for estimating the weathering process of rocks by carbonic, sulfate and nitrate acids. Through the calculation of the contribution ratio to $HCO_3{}^-$, the respective rates of carbonic, sulfate and nitrate contributions to DIC in the river water can be determined. This analysis aids in comprehending the extent of agricultural activities implicated in the weathering of carbonate rocks.

Equations (1)–(3) presented above represent the involvement of sulfuric and nitric acid in the dissolution reaction of carbonate rocks. Nevertheless, in the real world, dissolution does not strictly adhere to stoichiometric ratios. In calculations of the actual dissolution of carbonate rocks, molar coefficients can be used as assumptions. The specific process is as follows:

Let μ_1, μ_2, and μ_3 denote the respective moles of carbonic, sulfuric, and nitric acid participating in the dissolution reaction of carbonate rocks. The equation can be expressed as follows:

$$\mu_1Ca_{(1-x)}Mg_xCO_3 + \mu_1CO_2 + \mu_1H_2O \rightarrow \mu_1(1-x)Ca^{2+} + \mu_1xMg^{2+} + 2\mu_1HCO_3^- \quad (6)$$

$$2\mu_2Ca_{(1-x)}Mg_xCO_3 + \mu_2H_2SO_4 \rightarrow 2\mu_2(1-x)Ca^{2+} + 2\mu_2xMg^{2+} + 2\mu_2HCO_3^- + \mu_2SO_4^{2-} \quad (7)$$

$$\mu_3Ca_{(1-x)}Mg_xCO_3 + \mu_3HNO_3 \rightarrow \mu_3(1-x)Ca^{2+} + \mu_3xMg^{2+} + \mu_3HCO_3^- + \mu_3NO_3^- \quad (8)$$

Based on the provided reaction equation, the molar concentrations of SO_4^{2-}, NO_3^-, and HCO_3^- are known to be as follows:

$$\left[SO_4^{2-}\right] = \mu_2 \quad (9)$$

$$\left[NO_3^-\right] = \mu_3 \quad (10)$$

$$\left[HCO_3^-\right]_{carb} = 2\mu_1 + 2\mu_2 + \mu_3 \quad (11)$$

Equations (7)–(9) allow for the calculation of μ_1, where μ_1 is determined by the formula $\mu_1 = ([HCO_3^-] - 2[SO_4^{2-}] - [NO_3^-])/2$. The quantity of carbonate dissolved by carbonic acid μ1 can be determined by considering the concentrations of Ca^{2+}, SO_4^{2-}, and NO_3^- at sampling points. Subsequently, the dissolution ratios of carbonic, nitric, and sulfuric acid to carbonate rock at each sampling point can be calculated using the values of μ_1, μ_2, and μ_3. The calculations conducted for each sampling point yield the results depicted in Figure 9. Carbonic acid accounted for 87.77% to 94.55% of DIC, whereas sulfuric acid contributed 3.87% to 6.74%, and nitric acid contributed 0.28% to 5.96%. Notably, sulfuric acid exhibited a greater contribution than nitric acid. Within the Guancun Underground River Basin, the impact of agricultural activities on carbonate rock weathering follows the following order: GC3 > GC7 > GC8 > GC5 > GC4 > GC2 > GC1. GC8 serves as the main outlet of the Guancun Underground River Basin, where the upstream section receives water from the confluence of the main and tributary channels. This confluence results in the mixing of GC5 and GC7 ions as well as the dilution of water from the main and tributary streams. Except for GC8, Figure 1 illustrates a clear relationship between the size of depressions near the sampling sites and the extent of carbonate rock weathering caused by agricultural activities, with larger depression areas indicating a higher degree of weathering. The Guancun Underground River Basin exhibits a distinctive topographical pattern consisting of peaks and depressions, with the depressions serving as significant agricultural cultivation areas. The extent of agricultural activities is directly related to the size of these depressions, with larger areas indicating a higher proportion of agricultural practices. Moreover, the concentrations of SO_4^{2-} and NO_3^- significantly rise during the fertilization period of agricultural activities, thereby intensifying the degree of rock weathering.

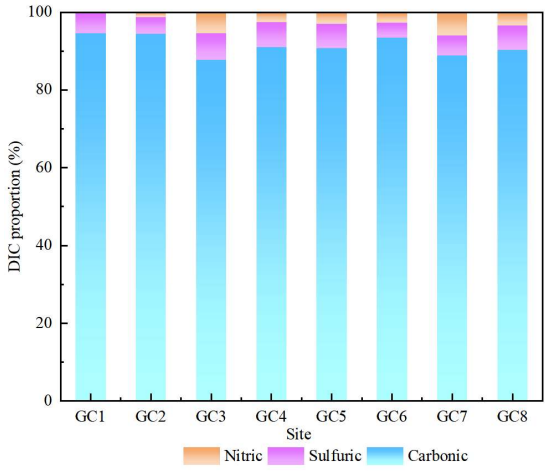

Figure 9. Proportion of DIC contributions from carbonic, nitric and sulfuric acid weathered carbonate rocks.

4.2. Carbon Isotope Verification of Carbonate Weathering by Sulfuric and Nitric Acid

Through the hydrochemical calculations discussed above, it is demonstrated that agricultural activities in the Guancun Underground River Basin generate sulfuric and nitric acid, both of which actively participate in the weathering of carbonate rocks. The dissolution of carbonate rocks by carbonic, sulfuric, and nitric acids contributes to the component

of DIC in the river water. To verify the involvement of sulfuric and nitric acid in carbonate rock weathering, carbon isotope analysis can be utilized. In the karst area of Maocun, Guilin City, the measured soil $\delta^{13}C_{DIC}$ values range from −29.35‰ to −18.26‰, with an average of −22.68‰. Studies on carbon isotope fractionation during gas-water exchange and CO_2 dissolution indicate that soil CO_2 dissolving in water at temperatures between 10 °C and 30 °C results in a fractionation of approximately −1.2‰ ± 0.05‰. Consequently, the $\delta^{13}C_{DIC}$ of dissolved soil CO_2 is approximately −23.88‰ [31,46–49]. Carbon isotope tests reveal a $\delta^{13}C_{DIC}$ value of −0.06‰ for carbonate rocks in the Lijiang basin [31,48,50]. Equation (1) illustrates that HCO_3^- formed during carbonate rock weathering has two sources: half from soil CO_2 and half from carbonate rocks. The DIC generated in this process comprises equal proportions of dissolved CO_2 ($\delta^{13}C_{DIC}$ = −23.88‰) and carbonate ($\delta^{13}C_{DIC} \approx -0.06$‰), resulting in an approximate $\delta^{13}C_{DIC}$ of −11.97‰. As it attains equilibrium with the dissolved isotopes, it will shift towards negative values of approximately −13.5‰ ± 1.1‰. The HCO_3^- resulting from the weathering of carbonate rocks by sulfuric and nitric acid, originating from agricultural activities as denoted by Equations (2) and (3), comes exclusively from carbonate minerals, yielding a $\delta^{13}C_{DIC}$ of approximately −0.06‰. An end-member hybrid model can be employed to estimate the $\delta^{13}C_{DIC}$ of the Guancun Underground River Basin using the following formula:

$$\delta^{13}C_{DIC-esti} = f_{sulf}^{13}C_{sulf} + f_{carb}^{13}C_{carb} \quad (12)$$

where f_{carb} and f_{sulf} as the fractions of DIC contribution from carbonic acid-induced carbonate weathering and sulfuric/nitric acid-induced carbonate weathering, respectively. $\delta^{13}C_{DIC\text{-}esti}$ denotes the estimated value derived from the mixed model.

Figure 10 presents the comparison between the estimated $\delta^{13}C_{DIC\text{-}esti}$ values obtained from the end-member hybrid model and the measured $\delta^{13}C_{DIC}$ values. The measured and estimated values at each sampling location exhibit close agreement, indicating the accuracy of hydrochemical methods in quantifying the contribution of sulfuric and nitric acid, resulting from agricultural activities, to carbonate rock weathering. The measured $\delta^{13}C_{DIC}$ values generally show slightly more negative values compared to the estimated $\delta^{13}C_{DIC\text{-}esti}$ values. Fluctuations in $\delta^{13}C_{DIC}$ in the Guancun Underground River Basin are attributed to the presence of phytoplankton and their photosynthesis and respiration processes. Photosynthesis utilizes dissolved $^{12}CO_2$, causing a positive shift in $\delta^{13}C_{DIC}$ values, while respiration releases $^{12}CO_2$, leading to a negative shift. Although photosynthesis and respiration are interconnected, they do not reach perfect equilibrium. It is important to consider the biogeochemical processes occurring in the system when interpreting the fluctuations in $\delta^{13}C_{DIC}$.

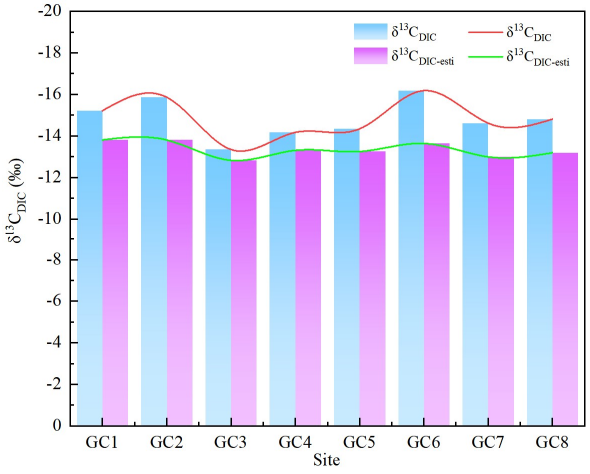

Figure 10. Plots of $\delta^{13}C_{DIC}$ and $\delta^{13}C_{DIC-esti}$ for each sampling point.

4.3. The Impact of Agricultural Activities on Carbon Sink in Karst Processes

Hydrochemical methods, based on the principle of mass conservation, are utilized to determine the weathering rates of carbonic, sulfuric, and nitric acid on carbonate rocks by employing ion ratios within basins. However, this method fails to incorporate inputs from human activities when assessing the carbon sink in the basin. In the weathering process of carbonate rocks, carbonic acid alone contributes to the carbon sink, whereas activities related to agriculture, such as the weathering of sulfuric and nitric acid, do not consume CO_2. The application of fertilizers has the potential to increase the mineralization of soil organic matter. For example, nitrogen-rich fertilizers can enhance microbial activity in the soil, leading to soil acidification. This acidification is subsequently neutralized by soil inorganic carbon. This process accelerates the decomposition of soil organic matter, releasing CO_2 and dissolved organic carbon (DOC) [51]. The amount and ratio of nitrogen and phosphorus released into downstream water bodies are influenced by the soil's nitrogen and phosphorus content and their release efficiency [52]. In karst regions, where the average soil layer thickness is approximately 50 cm, these dynamics are particularly significant. Studies have documented significant increases in DOC flux from agricultural soils following fertilizer application, indicating a direct link between fertilization practices and carbon loss. The Guancun Underground River Basin exhibits PCD landforms, and agricultural activities serve as the primary influencing factor. Hence, when evaluating the carbon sink process, it is crucial to consider the impact of agricultural activities, rendering the aforementioned hydrochemical method inapplicable. The contribution rates of SO_4^{2-} and NO_3^- to DIC in the Guancun Underground River originate from agricultural activities. The hydrochemical-runoff method is employed to assess the impact of agricultural activities on the karst carbon sink. Assuming that all HCO_3^- is derived from the weathering of carbonate rocks, unaffected by sulfuric and nitric acid, HCO_3^- can be attributed to half of the atmospheric CO_2 concentration, i.e., $[CO_2] = 1/2[HCO_3^-]$. The calculation of the carbon sink in the basin using the hydrochemical-runoff method is expressed by Equation (13):

$$\mathrm{CSF} = \frac{1}{2} \times 44 \times \frac{Q}{A} \times \left[\mathrm{HCO_3^-}\right]_{river} \tag{13}$$

where CSF is the flux of carbon sink ($t/km^2 \cdot a$); Q is the total annual runoff volume (m^3/a); A is the basin area (km^2); $[HCO_3^-]_{river}$ is the molar concentration of HCO_3^- in the water (mmol/L), and 44 is the relative molecular weight of CO_2.

Due to agricultural activities, sulfuric and nitric acids are involved in the dissolution of carbonate rocks. The formula for calculating the net carbon sink flux (NCSF), which takes into account the effects of sulfuric and nitric acid generated by agricultural activities, is modified based on Equations (2) and (3) and can be expressed as follows:

$$\begin{aligned} NCSF &= \frac{44}{A}\int_{t_1}^{t_2} Q \times \left(\frac{1}{2}\left[\mathrm{HCO_3^-}\right]dt - \left[SO_4^{2-}\right]dt - \frac{1}{2}\left[NO_3^-\right]dt\right) \\ &= \frac{44}{A}\sum_{t_1}^{t_2} Q_t \times \left(\frac{1}{2}\left[\mathrm{HCO_3^-}\right]_t - \left[SO_4^{2-}\right]_t - \frac{1}{2}\left[NO_3^-\right]_t\right) \end{aligned} \tag{14}$$

where $NCSF$ is the net carbon sink flux ($t/km^2 \cdot a$); Q is the flow rate (m^3/a); A is the basin area (km^2); $[HCO_3^-]$ is the molar concentration of HCO_3^- in the water (mmol/L); $[SO_4^{2-}]$ and $[NO_3^-]$ represent the molar concentrations of SO_4^{2-} and NO_3^- in the water (mmol/L). The value 44 represents the relative molecular weight of CO_2.

The Guancun Underground River Basin has a basin area of 30.5 km^2 and a flow rate of 20.28×10^6 m^3/a. The calculated results for the flux of carbon sinks were carried out both without considering the influence of agricultural activities and taking this influence into account. The values obtained are 71.87 $t/(km^2 \cdot a)$ and 61.91 $t/(km^2 \cdot a)$, respectively. The ratio of net carbon sink to carbon sink is 86.14%, indicating that approximately 13.86% of the carbon sink can be attributed to the contribution of sulfuric and nitric acid generated by agricultural activities to DIC. It is important to note that these activities do not consume

CO_2 from the atmosphere or soil, and thus, it should be deducted when calculating the overall carbon sink.

The presence of agricultural activities affects the composition of HCO_3^- in groundwater, which is not solely derived from the weathering of carbonate rocks but also involves the absorption of CO_2 from the atmosphere or soil. Moreover, a small fraction of HCO_3^- is generated through the weathering of carbonate rocks by acids produced from agricultural activities. In the Guancun Underground River, the average concentration of HCO_3^- is 4.91 mmol/L, with 86.14% contributed by the carbonic acid of carbonate rock weathering and 13.86% contributed by the sulfuric and nitric acid weathering of carbonate rocks caused by agricultural activities. Consequently, when assessing the carbon sink flux in karst basins located in PCD areas, it is crucial to consider the impact of agricultural activities.

Different karst basins and landforms, along with various land use types, exhibit varying influencing factors, which result in different contributions of sulfuric and nitric acid to DIC. Comparisons with three other karst types within the Southwest region of China. Hydrochemical data from the high mountain karst Jinfo Mountain karst spring [42] and the trough valley karst Qingmuguan and Nanshan Laolongdong underground rivers were utilized for analysis, as outlined in Figure 11. Observations indicate that karst basins primarily influenced by agricultural activities exhibit relatively low contributions of sulfuric and nitric acid to DIC. Conversely, areas influenced by tourism activities and urban development, characterized by higher population density and frequent human activities, demonstrate a greater contribution of sulfuric and nitric acid to DIC. Jinfo Mountain karst spring, officially certified as a 5A tourist attraction by the Chinese government, experiences periodic surges in visitor numbers. However, due to its unique geographical location, the construction of Medicine Pond Dam, a reservoir atop the mountain, has resulted in wastewater discharge that impacts the DIC contribution. Consequently, it exhibits the highest contribution of sulfuric and nitric acids to DIC [53]. The Nanshan Laolongdong Underground River Basin is undergoing rapid urbanization, is primarily used for residential construction, and features a widespread population distribution and mining areas. With relatively weak surface runoff, groundwater replenishment occurs mainly through sink holes, karst depressions, and karst fissures influenced by precipitation and surface sewage. As a result, this underground river is significantly influenced by human activities. The Qingmuguan Underground River Basin, characterized by its small area, mainly consists of dryland and paddy fields, accounting for approximately 34.73% of the entire basin. The agricultural fertilizers employed include amino nitrogen fertilizer, nitrogen-phosphorus compound fertilizer, potassium fertilizer, animal manure, and sulfur-containing pesticide sprays. In the Guancun Underground River Basin, the cultivated land area accounts for 12.58% of the total land area, which is 22.15% smaller than the proportion in the Qingmuguan Underground River Basin. Unexpectedly, the contribution of sulfuric and nitric acids to DIC is 20.61% lower. This suggests that the impact of agricultural activities on the karst carbon sink is correlated with the cultivated land area, whereby larger areas and higher fertilizer applications exert a greater influence on the carbon sink. The utilization of land is influenced by karst landforms and geological conditions, and humans develop and utilize the land based on locally suitable conditions, indirectly affecting the carbon sink. Thus, this portion should be excluded for an accurate calculation of the carbon sink.

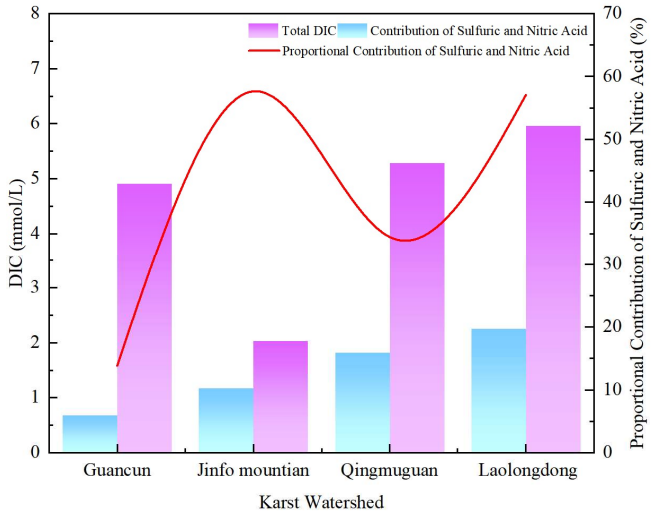

Figure 11. Contribution of sulfuric acid and nitric acid to the DIC in different basins.

5. Conclusions

In the PCD landform of Guancun, the Cl^-, SO_4^{2-}, and NO_3^- ions in the Underground River Basin exhibit consistent trends, spatial distribution, and sources. Based on ion correlation analysis using hydrochemical methods, these ions primarily originate from agricultural activities. Using isotopic methods, the sources of $\delta^{15}N\text{-}NO_3^-$ and $\delta^{18}O\text{-}NO_3^-$ were analyzed and identified as originating from NH_4^+ fertilizers and soil organic nitrogen in agricultural activities. Approximately 13.86% of the DIC in the basin originates from the weathering of carbonate rocks by sulfuric and nitric acid arising from agricultural activities. This process does not involve CO_2 consumption, thereby lacking a carbon sink mechanism, resulting in a reduction of carbon sink by 9.96 t/(km^2·a). The size of the depression where the sampling sites are located is related to the degree of carbonate rock weathering induced by agricultural activities. Larger depression areas are associated with greater proportions of agricultural cultivation, leading to increased carbonate rock weathering and reduced net carbon exchange rates. Comparing the contribution of sulfuric and nitric acid to DIC in karst basins with different land use types, such as the subalpine landform of Jinfo Mountain, the trough and valley landform of Qingmuguan, and the Nanshan Laolongdong underground rivers, agricultural activities are found to have less contribution to DIC, whereas tourism and urban activities contribute more to DIC. Analysis of the impact that karst basins have on inorganic carbon sinks provides valuable insights for accurately assessing carbon sink flux and offers a theoretical reference for quantifying the karst carbon sink in diverse types and regions. Moreover, this analysis enhances our understanding of the global carbon cycle mechanism, playing a crucial role in striving to achieve carbon peaking by 2030 and working towards carbon neutrality by 2060.

Author Contributions: Conceptualization, Q.X. and C.Z.; data curation, N.Z. and F.C.; methodology, N.Z., P.S. and Y.G.; validation, N.Z. and Y.M.; visualization, N.Z.; writing—original draft, N.Z.; writing—review and editing, Q.X., C.Z. and N.Z. All authors have read and agreed to the published version of the manuscript.

Funding: This work was supported by the Basic Research Fund Project of the National Key Research and Development Program [2020YFE0204700]; the Science and Technology Plan Project of Guangxi Province [2022GXNSFAA035604, 2022GXNSFAA035572, 2023GXNSFAA026473, GuikeAB22035010]; the Institute of Karst Geology, Chinese Academy of Geological Sciences [2021001, 2023019]; the China Geological Survey [DD20230547]; and China Foreign Experts Bureau Project (DL2023055001L).

Data Availability Statement: The data that support the findings of this study are available upon request from the corresponding author.

Acknowledgments: We thank the anonymous reviewers for their constructive comments.

Conflicts of Interest: The authors declare no conflicts of interest.

References

1. Kogan, F. *The IPCC Reports on Global Warming and Land Changes*; Springer International Publishing: Cham, Switzerland, 2023; pp. 67–79, ISBN 978-3-030-96809-0.
2. Du, X. Thoughts on Strategies and Paths to Achieve Carbon Peaking and Carbon Neutrality in China. *Front. Energy* **2023**, *17*, 324–331. [CrossRef]
3. Liu, X.; Wang, X.; Meng, X. Carbon Emission Scenario Prediction and Peak Path Selection in China. *Energies* **2023**, *16*, 2276. [CrossRef]
4. Li, L.; Huang, F.; Cao, J.; Pei, W.; Liang, Y. Carbon Sinks Flux Mechanism Analysis in Different Geological Background. *Adv. Mater. Res.* **2012**, *616–618*, 1528–1531. [CrossRef]
5. Sun, P.; He, S.; Yu, S.; Pu, J.; Yuan, Y.; Zhang, C. Dynamics in Riverine Inorganic and Organic Carbon Based on Carbonate Weathering Coupled with Aquatic Photosynthesis in a Karst Catchment, Southwest China. *Water Res.* **2021**, *189*, 116658. [CrossRef]
6. Wu, Y.; Wu, Y. The Increase in the Karstification–Photosynthesis Coupled Carbon Sink and Its Implication for Carbon Neutrality. *Agronomy* **2022**, *12*, 2147. [CrossRef]
7. An, R.; Liu, J.; Gao, Z.; Li, C.; Peng, Y. Hydrochemical Characterization, Controlling Factors and Water Quality of Surface Water in Shandong Province, North China. *J. Earth Sci.* **2024**, *35*, 155–166. [CrossRef]
8. Wang, K.-L.; Zhang, C.; Yue, Y.; Zhang, W.; Zhang, M.-Y.; Qi, X.; Fu, Z. Karst Landscapes of China: Patterns, Ecosystem Processes and Services. *Landsc. Ecol.* **2019**, *34*, 2743–2763. [CrossRef]
9. Goldscheider, N.; Chen, Z.; Auler, A.; Bakalowicz, M.; Broda, S.; Drew, D.; Hartmann, J.; Jiang, G.; Moosdorf, N.; Stevanovic, Z.; et al. Global Distribution of Carbonate Rocks and Karst Water Resources. *Hydrogeol. J.* **2020**, *28*, 1661–1677. [CrossRef]
10. Liu, Z.; Dreybrodt, W.; Wang, H. A New Direction in Effective Accounting for the Atmospheric CO_2 Budget: Considering the Combined Action of Carbonate Dissolution, the Global Water Cycle and Photosynthetic Uptake of DIC by Aquatic Organisms. *Earth-Sci. Rev.* **2010**, *99*, 162–172. [CrossRef]
11. Martin, J.B. Carbonate Minerals in the Global Carbon Cycle. *Chem. Geol.* **2017**, *449*, 58–72. [CrossRef]
12. Liu, J.; Han, G. Effects of Chemical Weathering and CO_2 Outgassing on δ13CDIC Signals in a Karst Watershed. *J. Hydrol.* **2020**, *589*, 125192. [CrossRef]
13. Zhou, G.; Bin, J.; Tao, X.; Yan, H. Estimation of Karst Carbon Sink and Its Contribution to CO_2 Emissions over a Decade Using Remote Sensing Imagery. *Appl. Geochem.* **2020**, *121*, 104689. [CrossRef]
14. Jia, B.; Zhou, G. Estimation of Global Karst Carbon Sink from 1950s to 2050s Using Response Surface Methodology. *Geo-Spat. Inf. Sci.* **2023**, *16*, 1–18. [CrossRef]
15. Chen, M.; Li, Y.; Tang, F.; Xu, Q.; Yu, M.; Zhang, H.; Li, X. Transformation of Paddy Field Use in Intermountain-Type Basins Using Evidence from the Structure and Function Perspective of Karst Mountain Areas in Southwest China. *Agronomy* **2023**, *13*, 1552. [CrossRef]
16. Feng, T.; Chen, H.; Polyakov, V.O.; Wang, K.; Zhang, X.; Zhang, W. Soil Erosion Rates in Two Karst Peak-Cluster Depression Basins of Northwest Guangxi, China: Comparison of the RUSLE Model with 137Cs Measurements. *Geomorphology* **2016**, *253*, 217–224. [CrossRef]
17. Wang, J.; Wei, H.; Huang, J.; He, T.; Deng, Y. Soil Aggregate Stability and Its Response to Overland Runoff–Sediment Transport in Karst Peak–Cluster Depressions. *J. Hydrol.* **2023**, *620*, 129437. [CrossRef]
18. Perrin, A.-S.; Probst, A.; Probst, J.-L. Impact of Nitrogenous Fertilizers on Carbonate Dissolution in Small Agricultural Catchments: Implications for Weathering CO_2 Uptake at Regional and Global Scales. *Geochim. Cosmochim. Acta* **2008**, *72*, 3105–3123. [CrossRef]
19. Raymond, P.A.; Hamilton, S.K. Anthropogenic Influences on Riverine Fluxes of Dissolved Inorganic Carbon to the Oceans. *Limnol. Oceanogr. Lett.* **2018**, *3*, 143–155. [CrossRef]
20. Xie, Y.; Huang, F.; Yang, H.; Yu, S. Role of Anthropogenic Sulfuric and Nitric Acids in Carbonate Weathering and Associated Carbon Sink Budget in a Karst Catchment (Guohua), Southwestern China. *J. Hydrol.* **2021**, *599*, 126287. [CrossRef]
21. Xu, S.; Li, S.; Su, J.; Yue, F.; Zhong, J.; Chen, S. Oxidation of Pyrite and Reducing Nitrogen Fertilizer Enhanced the Carbon Cycle by Driving Terrestrial Chemical Weathering. *Sci. Total Environ.* **2021**, *768*, 144343. [CrossRef] [PubMed]
22. Bukaveckas, P.A.; Barisevičiūtė, R.; Zilius, M.; Vybernaite-Lubiene, I.; Petkuviene, J.; Vaiciute, D.; Zemlys, P. Carbon Fluxes from River to Sea: Sources and Fate of Carbon in a Shallow, Coastal Lagoon. *Estuaries Coasts* **2023**, *46*, 1223–1238. [CrossRef]
23. Huang, Q.; Qin, X.; Liu, P.; Zhang, L.; Su, C. Impact of Sulfuric and Nitric Acid on Carbonate Dissolution, and the Associated Deficit of CO_2 Uptake in the Upper–Middle Reaches of the Wujiang River, China. *J. Contam. Hydrol.* **2017**, *203*, 18–27. [CrossRef] [PubMed]
24. Yu, S.; He, S.; Sun, P.; Pu, J.; Huang, J.; Luo, H.; Li, Y.; Li, R.; Yuan, Y. Impacts of Anthropogenic Activities on Weathering and Carbon Fluxes: A Case Study in the Xijiang River Basin, Southwest China. *Environ. Earth Sci.* **2016**, *75*, 589. [CrossRef]

25. Yuan, Y.-Q.; Sun, P.-A.; Su, Z.; Yu, S.; Zhong, L.-H.; He, S.-Y.; Xu, Q. Dynamic Changes in Hydrochemical Characteristics and Influencing Factors in the Karst Watershed Flood Process. *Huan Jing Ke Xue = Huanjing Kexue* **2019**, *40*, 4889–4899. [CrossRef] [PubMed]
26. Raymond, P.A.; Oh, N.-H.; Turner, R.E.; Broussard, W. Anthropogenically Enhanced Fluxes of Water and Carbon from the Mississippi River. *Nature* **2008**, *451*, 449–452. [CrossRef] [PubMed]
27. Zhang, Y.; Jiang, Y.; Yuan, D.; Cui, J.; Li, Y.; Yang, J.; Cao, M. Source and Flux of Anthropogenically Enhanced Dissolved Inorganic Carbon: A Comparative Study of Urban and Forest Karst Catchments in Southwest China. *Sci. Total Environ.* **2020**, *725*, 138255. [CrossRef] [PubMed]
28. Zhu, H.; Wu, L.; Xin, C.; Yu, S.; Guo, Y.; Wang, J. Impact of Anthropogenic Sulfate Deposition via Precipitation on Carbonate Weathering in a Typical Industrial City in a Karst Basin of Southwest China: A Case Study in Liuzhou. *Appl. Geochem.* **2019**, *110*, 104417. [CrossRef]
29. Zhao, G.; Huang, Q.; Zhu, Y.; Xu, Y.; Pu, Z. Simulation of the Buffering Process of Karst Soil on Sulfuric Acid Rain and the Characteristic of $\delta^{13}C_{DIC}$ and the Carbon Sink Flux in Guilin City, Southwest China. *Environ. Earth Sci.* **2023**, *82*, 296. [CrossRef]
30. Anderson, S.P.; Drever, J.I.; Frost, C.D.; Holden, P. Chemical Weathering in the Foreland of a Retreating Glacier. *Geochim. Cosmochim. Acta* **2000**, *64*, 1173–1189. [CrossRef]
31. Jiang, Y.; Hu, Y.; Schirmer, M. Biogeochemical Controls on Daily Cycling of Hydrochemistry and δ13C of Dissolved Inorganic Carbon in a Karst Spring-Fed Pool. *J. Hydrol.* **2013**, *478*, 157–168. [CrossRef]
32. Sun, P.; Yu, S.; Mo, F.; He, S.; Lu, J.; Yuan, Y. Hydrochemical Characteristics and Influencing Factors in Different Geological Background: A Case Study in Darongjiang and Lingqu Basin, Guangxi, China. *Huan Jing Ke Xue* **2016**, *37*, 123–131.
33. Wang, Q.; Yu, S.; Jiang, P.-P.; Sun, P.-A. Water Chemical Characteristics and Influence of Exogenous Acids in the Yangtze River Basin. *Huan Jing Ke Xue = Huanjing Kexue* **2021**, *42*, 4687–4697. [CrossRef]
34. Cao, J.; Wu, X.; Huang, F.; Groves, C.; Yang, H.; Zhang, C. Global Significance of the Carbon Cycle in the Karst Dynamic System: Evidence from Geological and Ecological Processes. *China Geol.* **2018**, *1*, 17–27. [CrossRef]
35. Zhao, R.; Liu, Z.; Dong, L.; Zhang, Q.; Liu, C. The Fates of CO_2 Generated by H_2SO_4 and/or HNO_3 during the Dissolution of Carbonate and Their Influences on the Karst-Related Carbon Cycle. *J. Hydrol.* **2020**, *597*, 125746. [CrossRef]
36. Huang, K.; Ma, Z.; Wang, X.; Shan, J.; Zhang, Z.; Pinhua, X.; Jiang, X.; Wu, X.; Huang, X. Control of Soil Organic Carbon under Karst Landforms: A Case Study of Guizhou Province, in Southwest China. *Ecol. Indic.* **2022**, *145*, 109624. [CrossRef]
37. Zhao, R.; Han, Z.W.; Shen, C.H.; Zhang, S.; Tu, H.; Guo, Y.L. Identifying Nitrate Sources in a Typical Karst Underground River Basin. *Huan Jing Ke Xue = Huanjing Kexue* **2020**, *41*, 2664–2670. [CrossRef]
38. Fang, G.; Guanghui, J.; Daoxian, Y. Change of Major Ions Concentration in Subterranean River in Karst Areas in South China. *Water Resour. Prot.* **2008**, *24*, 16–19.
39. Zhang, L.; Qin, X.; Huang, Q.; Liu, P. Role of Sulfuric Acid in Chemical Weathering of Carbonate Rocks for Evaluating of Carbon Sinks in the Yangtze River Basin, China. *E3S Web Conf.* **2019**, *98*, 06015. [CrossRef]
40. Guo, F.; Jiang, G.; Kang, Z. Comparative study on carbon sink effects of typical subtropical karst water systems. *Carsologica Sin.* **2011**, *30*, 403–409. (In Chinese)
41. Pu, J.; Li, J.; Khadka, M.B.; Martin, J.B.; Zhang, T.; Yu, S.; Yuan, D. In-Stream Metabolism and Atmospheric Carbon Sequestration in a Groundwater-Fed Karst Stream. *Sci. Total Environ.* **2017**, *579*, 1343–1355. [CrossRef]
42. Shen, C.; Han, Z.; Guo, Y.; Zhang, S.; Tu, H.; Guo, F. Temporal and Spatial Distribution Characteristics and Factors Influencing Nitrate Level in Waters of a Typical Karst Underground River System. *Chin. J. Eco-Agric.* **2019**, *27*, 1255–1264. [CrossRef]
43. Al Bassam, A.; Khalil, A. DurovPwin: A New Version to Plot the Expanded Durov Diagram for Hydro-Chemical Data Analysis. *Comput. Geosci.* **2012**, *42*, 1–6. [CrossRef]
44. Ravikumar, P.; Somashekar, R.K.; Prakash, K. A Comparative Study on Usage of Durov and Piper Diagrams to Interpret Hydrochemical Processes in Groundwater from SRLIS River Basin, Karnataka, India. *Elixir Earth Sci.* **2015**, *80*, 31073–31077.
45. Hinckley, E.-L.S.; Crawford, J.T.; Fakhraei, H.; Driscoll, C.T. A Shift in Sulfur-Cycle Manipulation from Atmospheric Emissions to Agricultural Additions. *Nat. Geosci.* **2020**, *13*, 597–604. [CrossRef]
46. Davidson, G.R. The Stable Isotopic Composition and Measurement of Carbon in Soil CO_2. *Geochim. Cosmochim. Acta* **1995**, *59*, 2485–2489. [CrossRef]
47. Pan, G.; He, S.; Cao, J.; Tao, Y.; Sun, Y. Variation of δ 13 C in Karst Soil in Yaji Karst Experiment Site, Guilin. *Chin. Sci. Bull.* **2002**, *47*, 500–503. [CrossRef]
48. Cao, J.; Zhou, L.; Yang, H.; Lu, Q.; Kang, Z. Comparison of Carbon Transfer between Forest Soils in Karst and Clasolite Areas and the Karst Carbon Sink Effect in Maocun Village of Guilin. *Quat. Sci.* **2011**, *31*, 431–437.
49. Jia, G.-D.; Chen, F.-J.; Deng, W.-F. Seasonal Variations of Dissolved Inorganic Carbon Isotope in the Beijiang River. *Diqiu Kexue-Zhongguo Dizhi Daxue Xuebao/Earth Sci. -J. China Univ. Geosci.* **2012**, *37*, 365–369.
50. Telmer, K.; Veizer, J. Carbon Fluxes, pCO_2 and Substrate Weathering in a Large Northern River Basin, Canada: Carbon Isotope Perspectives. *Chem. Geol.* **1999**, *159*, 61–86. [CrossRef]
51. Raza, S.; Miao, N.; Wang, P.; Ju, X.; Chen, Z.; Zhou, J.; Kuzyakov, Y. Dramatic Loss of Inorganic Carbon by Nitrogen-Induced Soil Acidification in Chinese Croplands. *Glob. Chang. Biol.* **2020**, *26*, 3738–3751. [CrossRef] [PubMed]

52. Liu, J.; Wang, Y.; Li, Y.; Peñuelas, J.; Zhao, Y.; Sardans, J.; Tetzlaff, D.; Liu, J.; Liu, X.; Yuan, H.; et al. Soil Ecological Stoichiometry Synchronously Regulates Stream Nitrogen and Phosphorus Concentrations and Ratios. *CATENA* **2023**, *231*, 107357. [CrossRef]
53. Zhan, Z.-J.; Chen, F.; Yang, P.; Ren, J.; Zhang, H.-Y.; Liu, D.-W.; Lan, J.-C.; Zhang, Y. Comparison on the Hydrogeochemical Characteristics of Typical Karst Groundwater System in Southwest China, a Case of Qingmuguan and Laolongdong in Chongqing. *Huan Jing Ke Xue = Huanjing Kexue* **2016**, *37*, 3365–3374. [CrossRef] [PubMed]